Applied Surface Science 730 (2026) 166240

Contents lists available at ScienceDirect

Applied Surface Science

journal homepage: www.elsevier.com/locate/apsusc

Full Length Article

Reactive HiPIMS-deposited CrN_x coatings: plasma diagnostics and nitrogen incorporation

Kaiwei Yang [a,b,1], Yiqun Feng [a,1], Yuxing Qi [a], Guanshui Ma [a], Zhenyu Wang [a], Aiying Wang [a,b,*]

[a] State Key Laboratory of Advanced Marine Materials, Zhejiang Key Laboratory of Extreme-environmental Material Surfaces and Interfaces, Ningbo Institute of Materials Technology and Engineering, Chinese Academy of Sciences, Ningbo 315201, China
[b] College of Materials Science and Opto-Electronic Technology, University of Chinese Academy of Sciences, Beijing 100049, China

ARTICLE INFO

Keywords:
HiPIMS
Reactive sputtering
CrN_x coating
Plasma diagnostics
Electron density
Nitrogen incorporation

ABSTRACT

Controlling nitrogen incorporation in CrN_x coatings deposited by reactive high-power impulse magnetron sputtering (HiPIMS) requires understanding the interplay between plasma-assisted kinetics and thermodynamic constraints. In this study, CrN_x coatings were deposited under metallic, transition, and compound sputtering modes using N_2 flow rates from 0 to 75 sccm. Plasma diagnostics revealed that increasing N_2 flow rate induces a transition from metallic to compound discharge, accompanied by an increase in discharge voltage and peak power density. Optical emission spectroscopy showed an enhanced Cr^+/Cr^* emission intensity ratio, indicating a plasma state enriched with energetic metal species. Coating characterization by EPMA, XPS, and XRD demonstrated that the nitrogen content increases with N_2 flow rate but saturates at approximately 52 at.%, which, within experimental uncertainty, is consistent with the stoichiometric limit of CrN defined by the Cr–N phase diagram. XPS further revealed a systematic shift of the N 1s binding energy toward higher values, indicating strengthened Cr-N bonding under energy-assisted growth conditions. These results show that while the maximum nitrogen content in CrN_x coatings is thermodynamically constrained, the intrinsically high-energy, metal-ion-dominated plasma generated by reactive HiPIMS effectively controls the kinetic pathway toward stoichiometric CrN, highlighting the advantages of HiPIMS for tailoring nitride coatings through energy-assisted deposition.

1. Introduction

Transition metal nitrides (TMNs) have been extensively employed as protective coatings in various industries, such as cutting tools, integrated circuit diffusion barrier, and marine anti-corrosion applications, due to their high hardness, excellent wear resistance and superior corrosion resistance [1–4]. Among binary TMNs, CrN coatings stand out for their exceptional corrosion resistance, oxidation resistance and fretting wear resistance [5]. Several methods are available for depositing CrN coatings, including chemical vapor deposition [6], arc ion plating [7], and reactive magnetron sputtering [8,9]. Among these, reactive magnetron sputtering is widely adopted because it enables a broad compositional range at low substrate temperatures by controlling the reactive gas flow [10].

In recent years, high power impulse magnetron sputtering (HiPIMS) has emerged as an advanced physical vapor deposition technique capable of generating dense, highly ionized plasmas with peak ionization densities on the order of 10^{19} m^{-3}, two to three orders of magnitude higher than those achieved in conventional DC magnetron sputtering (DCMS) [11]. The pulsed high-power nature of HiPIMS leads to enhanced ion bombardment, improved film density, and superior adhesion, even at low substrate temperatures [12,13]. Nonetheless, the incorporation of reactive gases such as N_2 into HiPIMS discharges introduces additional complexity. The presence of reactive species alters the plasma chemistry, electron energy distribution, and target surface condition, all of which influence ionization pathways and the resultant film growth kinetics [14,15].

Despite extensive studies, the interpretation of hysteresis behavior in reactive HiPIMS remains a topic of debate. The interplay between target poisoning, plasma composition, and reactive gas dynamics is far from

* Corresponding author at: State Key Laboratory of Advanced Marine Materials, Zhejiang Key Laboratory of Extreme-environmental Material Surfaces and Interfaces, Ningbo Institute of Materials Technology and Engineering, Chinese Academy of Sciences, Ningbo 315201, China.
E-mail address: aywang@nimte.ac.cn (A. Wang).
[1] These authors contributed equally to this work.

https://doi.org/10.1016/j.apsusc.2026.166240
Received 29 October 2025; Received in revised form 4 February 2026; Accepted 6 February 2026
Available online 11 February 2026

fully understood [16]. Recent investigations have shown that the ionization of nitrogen and metal species strongly depends on the discharge mode and instantaneous plasma parameters, such as electron temperature and ion density [2]. However, the direct correlation between plasma characteristics and nitrogen incorporation efficiency in CrN coatings is still insufficiently clarified. The CrN_x system exhibited a hysteresis loop with a relatively sharp transition region, indicating a change in process stability with N_2 flow rate [17]. In particular, it remains unclear how the variation of plasma parameters with nitrogen flow rate governs the kinetics and thermodynamic limits of nitrogen uptake during CrN_x film formation.

Plasma diagnostics is an effective approach to gain insight into how plasma parameters affect coating formation at the microscopic level. Macak et al. [18] were among the first to use optical emission spectroscopy (OES) to study the composition and temporal evolution of HiPIMS plasma, demonstrating its utility for monitoring ionized species. Vetushka et al. [19] employed Langmuir probe measurements to examine plasma parameters in HiPIMS discharges, revealing a strong dependence of plasma density on the target material. These diagnostic techniques, when applied to reactive environments, can provide valuable insights into the complex interplay between gas-phase chemistry and film growth.

The microstructural features of CrN_x coatings deposited by magnetron sputtering and HiPIMS, including dense columnar growth, grain refinement, and phase formation mechanisms, have been well documented using transmission electron microscopy [20,21]. These studies have yielded important insights into the structure–property relationships of Cr–N coatings. Despite this progress, the link between plasma conditions and nitrogen incorporation during reactive HiPIMS is still not well understood. In particular, plasma diagnostics are rarely directly correlated with nitrogen content and phase evolution, limiting the ability to separate kinetic effects from thermodynamic constraints in the Cr–N system.

In this work, key plasma parameters, including electron density, electron temperature, and excited species, are systematically linked to nitrogen incorporation and phase evolution in CrN_x coatings deposited by reactive HiPIMS. By combining in situ plasma diagnostics with comprehensive coating characterization, this study elucidates the relative contributions of plasma-assisted kinetics and thermodynamic limits to the final coating composition.

2. Experimental details

2.1. Deposition processes

Fig. 1 shows the schematic diagram of the deposition system. CrN_x coatings were deposited on N-type 4H-SiC (0 0 0 1) single-crystal substrates (zero diffraction plate is made of Silicon cut at special orientation) using a HiPIMS system. The target material was chromium metal with a purity of 99.99 wt% and dimensions of 400 × 100 × 7 mm. Before deposition, the 4H-SiC (0001) substrates were sequentially cleaned using ultrasonic treatment in acetone and alcohol for 10 min each.

The deposition chamber was evacuated to a base pressure of 4×10^{-3} Pa over approximately 3 h. Prior to deposition, the substrates were Ar^+ ion-etched at 1 Pa for 30 min under a bias voltage of −200 V, effectively removing surface contaminants and partially thinning the native oxide layer. During deposition, the Ar (50 sccm) and N_2 (0–75 sccm) gas flow rates were controlled by mass flow controllers. The Ar flow rate and pumping speed were kept constant, and the chamber pressure evolved naturally with the total gas flow. Coatings were deposited at a constant average power of 3 kW using a SPIK 3000 A pulsed power supply (MELEC, Germany), with the ON/OFF time of 100/1900 μs (5% duty cycle). A negative bias voltage of −100 V was applied to the substrates during deposition. The distance between the target and the substrate was 12 cm, and the rotational speed of the substrate holder was 12 rpm to ensure uniform coating thickness.

Five series of CrN_x coatings were prepared in this study with N_2 flow rates of 0, 10, 30, 55, and 75 sccm, respectively. For all samples, an approximately 0.25 μm Cr transition layer was deposited. The deposition time for each sample was adjusted to achieve a uniform CrN_x coating thickness of 1.45 ± 0.25 μm, resulting in deposition rates of 27.37, 19.29, 15.18, 13.69, and 13.11 nm/min, respectively.

2.2. Monitoring of HiPIMS

The current and voltage were measured using a combined current transducer (LEM LT58-S7) and a high-voltage probe (UT-V23, UNI-T), respectively. The signals were recorded with a digital storage oscilloscope (Tektronix TDS 1012C-SC).

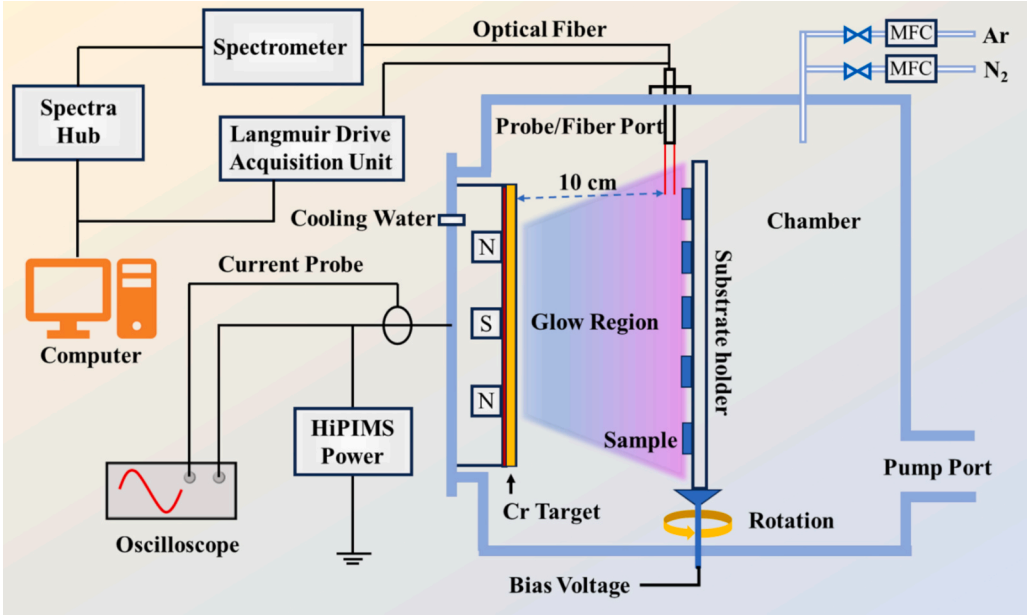

Fig. 1. Schematic diagram of deposition system and plasma diagnostics.

2.3. Coating characterization

The cross-sectional morphologies of the CrN_x coatings were examined using scanning electron microscopy (SEM, Hitachi S4800, Japan) at an accelerating voltage of 10 kV. Prior to imaging, the samples were mechanically fractured to expose their cross sections. Electron probe X-ray microanalysis (EPMA, JEOL JXA-iHP200F, Japan) was performed in circle mode with a sampling diameter of 3 μm, using an accelerating voltage of 15 kV and a beam current of 20 nA. For each coating, the elemental composition was determined by averaging the results obtained from five randomly selected measurement points on the coating surface to ensure compositional uniformity and measurement repeatability. The variation of atomic concentration (mol%) with coating thickness for samples S0 to S75 sccm was measured using a glow discharge optical emission spectrometer (GD-OES, Spectrum Analytik GmbH GDA 750HP, Germany). The elemental composition and binding energy of CrN_x coatings were determined using X-ray photoelectron spectroscopy (XPS, Kratos Axis Supra, UK) with an Al K_α X-ray source (1486.6 eV). Prior to XPS analysis, surface contamination was removed by Ar^+ ion etching at 5 kV for 3 min. The crystal structure of the samples was characterized by X-ray diffraction (XRD, Brucker D8 Discover, Germany) using a Cu K_α source ($\lambda = 1.5406$ Å) operated at 40 kV × 40 mA. A conventional $\theta/2\theta$ scan was performed with 2θ ranging from 20° to 90°.

2.4. Plasma diagnostics

The energetic species in the plasma were analyzed using an optical emission spectrometer (OES, Princeton Instruments SP-2500) equipped with a grating of 1200 groves/mm. The OES fiber port was positioned approximately 10 cm perpendicular to the sputtering region of the target surface. The detected spectra had a wavelength resolution of 1 nm and covered a range from 200 nm to 900 nm. SpectraSense software was used to collect, record, and process the spectral data.

A single Langmuir probe (Impedans Ltd, LP-500 ALP system) was vertically installed in the vacuum chamber to perform time-resolved measurements of plasma parameters near the substrate during the reactive HiPIMS discharge. The probe was made of tungsten, with a radius of 0.35 mm and an exposed length of approximately 5 mm. The I–V characteristic curve was plotted based on current and voltage measurements from the probe. From this curve, the plasma potential (V_p), electron density (n_e), ion density (n_i), electron temperature (T_e), and electron energy distribution function (EEDF) were analyzed and determined.

3. Results

3.1. Reactive HiPIMS discharge behavior in Ar/N_2 atmosphere

Fig. 2(a) shows the variation of the discharge voltage as a function of N_2 flow rate, exhibiting a clear hysteresis behavior during reactive Cr sputtering. An abrupt voltage transition is observed at approximately 40 sccm along the increasing flow branch, while a distinct return path appears during the decreasing flow sequence.

Fig. 2(b) and (c) show the discharge voltage and current waveforms for reactive HiPIMS of Cr under three different sputtering modes. To maintain a constant average discharge power, the discharge voltage (in Fig. 2b) was according to changes in the reactive gas flow rate. The discharge current waveform serves as a sensitive indicator of target surface composition and plasma processes in reactive HiPIMS [22]. In metallic mode, the current waveform exhibits a rapid rise followed by a gradual increase, forming a parabolic profile. In transition and compound modes, the current increases linearly before dropping to zero [16].

The peak power density of the CrN_x reactive HiPIMS ranged from 0.236 to 0.314 kW/cm^2, as listed in Table 1, which corresponds to a low-density discharge mode [23]. A brief delay of approximately 5 μs was observed in the target current during the initial stage of current pulses, indicating that the HiPIMS plasma was re-ignited at the beginning of each discharge period [24]. This delay is associated with the time required for the initial electrons to appear and initiate an avalanche ionization process [25].

3.2. Plasma diagnostics for reactive Cr HiPIMS

The composition of coatings produced by reactive sputtering depends on both the target surface condition and the plasma characteristics [10]. In this study, the plasma species generated during reactive HiPIMS deposition were monitored using OES. Table 2 lists the emission lines selected for analysis along with the corresponding energy levels involved in the transitions. Since ground state do not emit radiation, determining the absolute number densities of ground-state atoms and

Table 1
Discharge parameters under different N_2 flow rate.

Parameters	0 sccm	10 sccm	30 sccm	55 sccm	75 sccm
Average voltage of pulse-on (V)	643	673	684	711	725
Peak current (A)	146	157	177	186	182
Peak current density (A/cm^2)	0.37	0.39	0.44	0.47	0.45
Peak power density (kW/cm^2)	0.236	0.262	0.296	0.314	0.311

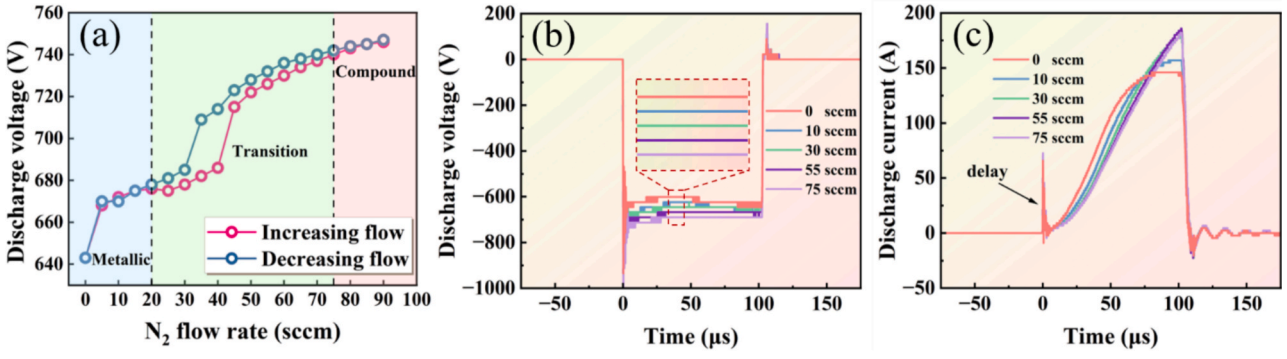

Fig. 2. (a) Discharge voltage hysteresis curves for Cr sputtering processes in Ar/N_2 atmosphere, (b) discharge voltage, and (c) current waveforms recorded under different N_2 flow rates.

Table 2
Spectroscopic data for emitted lines.

Species	Emitted wavelength (nm)	Transition	Upper level energy (eV)
Cr^+	284.1	$3d^4 4p(Z^4I^\circ) \rightarrow 3d^4 4a(a^4H)$	8.15
Cr*	425.6	$3d^5 4p(Y^7P^\circ) \rightarrow 3d^5 4s(a^7S)$	2.91
Ar^+	434.9	$3s^2 3p^4 4p \rightarrow 3s^2 3p^4 4s$	19.49
Ar*	720.9	$3s^2 3p^5 6s \rightarrow 3s^2 3p^5 4p$	15.02

ions from the emission spectra is challenging [26]. Therefore, a qualitative analysis of the spectral line intensities was conducted to estimate the types and relative abundances of excited atoms and ions in the plasma.

Fig. 3 presents the OES spectra of plasma species during deposition, showing characteristic emission lines of Cr* (426 nm), Ar* (721 nm), Cr^+ (284 nm), and Ar^+ (435 nm) [23,27]. The dominant active species were Cr* and Ar^+, with the Ar^+ line exhibiting significantly greater intensity than the Cr^+ line.

A comparison of the spectral intensity curves of Cr* (426 nm) and Ar^+ (435 nm) as a function of N_2 flow rate shows that the intensities of both species decrease monotonically with increasing N_2 flow, as illustrated in Fig. 4. Nitrogen-related emission lines could not be clearly resolved under the present measurement conditions. Under the constant power mode of the HiPIMS power supply, the introduction and progressive increase of N_2 flow result in an overall reduction in the measured emission intensities of the detected plasma species.

Fig. 4(c) summarizes the evolution of the Cr^+/Cr* intensity ratio with increasing N_2 flow rate. The Cr^+/Cr* ratio initially increases and subsequently decreases as the discharge transitions from metallic to compound mode. Notably, the ratio remains higher in the transition and compound modes compared to the metallic mode. This behavior reflects a slower decrease in Cr^+ emission intensity relative to that of Cr*, rather than an absolute increase in Cr^+ intensity.

It is worth noting that increasing the N_2 flow rate did not result in discernible changes in the plasma emission spectra, except for variations in intensity. No distinct emission lines attributable to excited nitrogen species were detected. This behavior can be explained by the well-known spectral overlap between molecular nitrogen emissions and strong Cr atomic lines in reactive Cr–N plasmas [28], as well as by the limited excitation and dissociation efficiency of N_2 under the present discharge conditions.

Within the primary CrN_x plasma spectral ranges (310–430 nm and 620–720 nm), the emission spectra were dominated by Cr-related lines,

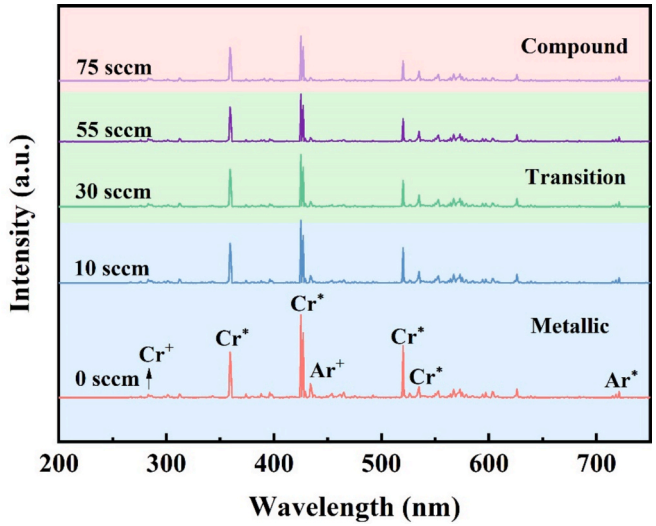

Fig. 3. OES in CrN_x plasma region under different sputtering modes.

while nitrogen-related emissions remained below the detection limit. This indicates that the excitation and dissociation of N_2 molecules were kinetically limited under the prevailing plasma conditions, which is consistent with the reduced electron density measured by the Langmuir probe, as discussed below.

Fig. 5(a) presents the time-averaged I–V characteristic curve measured using the Langmuir probe. From this curve, the V_p can be directly obtained as 0.91, 0.96, 0.97, 0.98 and 1.01, respectively. The relationship between the EEDF and the I-V characteristic curve is described by the Druyvesteyn formula [29,30]:

$$f(V) = \frac{2m_e}{Ae^2}\left(\frac{2eV}{m_e}\right)^{\frac{1}{2}}\frac{d^2I_e(V)}{dV^2}$$

where V, A, m_e, and I_e represent the probe voltage relative to plasma potential, probe area exposed to the plasma, electron mass, and probe current, respectively.

The electron energy distribution function (EEDF) in Fig. 5(b) exhibits a single-peak Maxwellian distribution with similar peak positions at low energies. As the N_2 flow rate increases, the population of high-energy electrons is noticeably enhanced, resulting in a more pronounced high-energy tail in the energy range of approximately 8–10 eV. Fig. 5(c) shows the variation of electron density (n_e) and effective electron temperature (T_{eff}) as a function of N_2 flow rate. The electron density decreases by approximately 33%, from 2.87×10^{16} m^{-3} in metallic mode (0 sccm) to 1.92×10^{16} m^{-3} in compound mode (75 sccm). In contrast, the effective electron temperature increases with increasing N_2 flow rate.

3.3. Chemical composition and microstructure of CrN_x coatings

Fig. 6 shows cross-sectional SEM morphologies of the Cr-N coatings deposited at different N_2 flow rates. All coatings exhibit a columnar growth structure. The nitrogen contents measured by EPMA at N_2 flow rates of 0, 10, 30, 55, and 75 sccm were 0, 28.2, 44.7, 52.0, and 52.5 at.%, respectively. The nitrogen content increases markedly with increasing N_2 flow rate and exhibits a clear saturation behavior close to ~52 at.% for flow rates above 55 sccm.

GD-OES depth profiles (Fig. 7) show that the atomic concentrations of Cr and N remain relatively constant throughout the coating thickness for all samples, indicating stable deposition conditions and good compositional uniformity across different sputtering modes. The nitrogen content determined by GD-OES increased from 0 at.% to 40.92 at.%, and then to 50.18 at.%, a trend consistent with the EPMA results.

Fig. 8 presents the XPS results detailing the phase evolution of CrN_x coatings. The peaks of Cr 2p and N 1s were fitted using the least squares method with a Gaussian-Lorentzian envelope [31]. The Cr $2p_{3/2}$ peak was deconvoluted into four components: Cr at 574 eV [32], Cr_2N at 575.8 ± 0.1 eV, CrN at 574.7 ± 0.1 eV [9,33], and Cr_2O_3 at 577.3 eV [34], as shown in Fig. 5(a). It is worth noting that the Cr_2N peak, with its elevated amplitude and energy position compared to values reported in the literature [9,33], may obscure the presence of chromium oxynitride (CrO_xN_y) at 575.7 ± 0.4 eV [35], indicating a possible overlap between the Cr_2N and CrO_xN_y peaks [34,36,37]. The N 1s peak can be deconvoluted into three primary sub-peaks: CrN at 396.8 ± 0.4 eV and Cr_2N at 397.4 ± 0.4 eV [38], as shown in Fig. 8(b), along with CrO_xN_y observed at 398.2 ± 0.4 eV.

The relative surface phase composition, estimated from the peak area ratios (Fig. 8d), shows that the CrN phase fraction increased from 13.73% (10 sccm) to over 77% (30 sccm, 55 sccm, and 75 sccm). This indicates that the transition from metallic to compound mode promotes the formation of the CrN phase. The elemental compositions derived from XPS are shown in Fig. 8(c), where the nitrogen content increases with increasing N_2 flow rate and saturates at approximately 37 at.%. In addition, the Cr-N related N 1s peak exhibits a gradual shift toward higher binding energy with increasing N_2 flow rate, increasing from

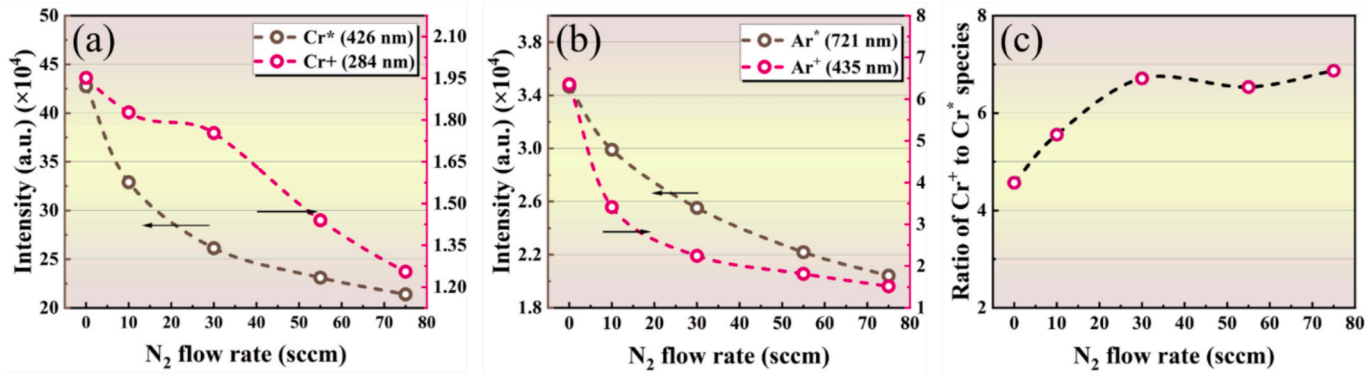

Fig. 4. (a) variations of Cr*(426 nm) and Cr^+(284 nm) spectral intensity, (b) variations of Ar*(721 nm) and Ar^+(435 nm) spectral intensity, (c) the proportion of Cr^+ to Cr* species.

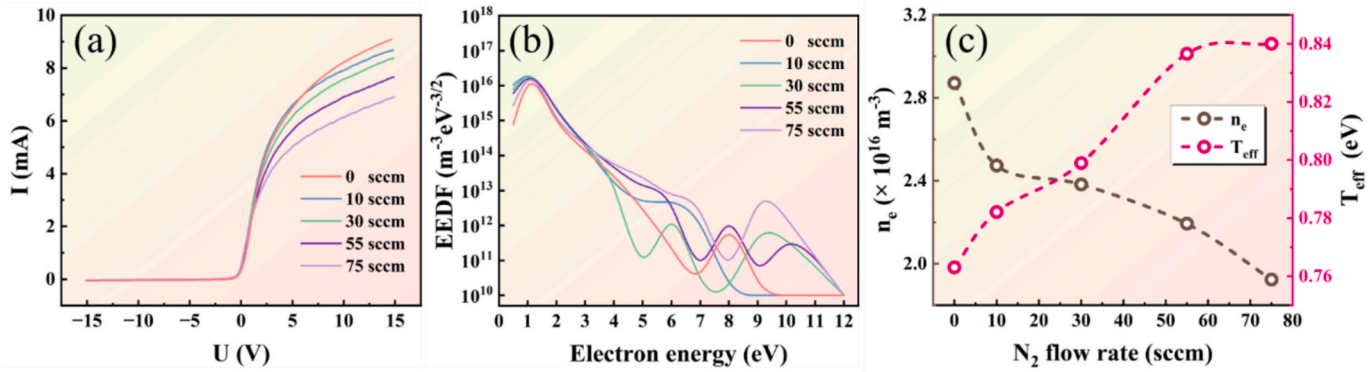

Fig. 5. Plasma parameter in different sputtering modes: (a) I-V characteristic, (b) electron energy distribution function, (c) electron density and electron temperature.

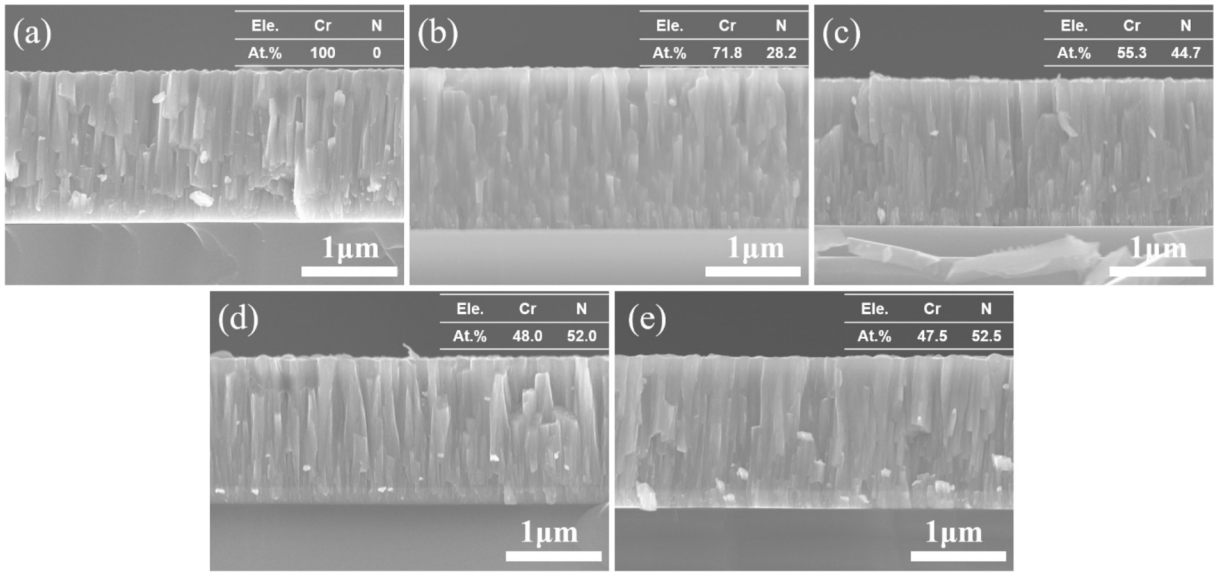

Fig. 6. Cross-section morphologies and EPMA-determined compositions of CrN_x coatings under different sputtering modes: (a) 0 sccm, (b) 10 sccm, (c) 30 sccm, (d) 55 sccm, and (e) 75 sccm.

~396.4 eV at 10 sccm to ~396.6 eV at 30 sccm and further to ~396.8 eV at 75 sccm. This progressive binding energy increase suggests enhanced charge transfer from Cr to N and a strengthening of Cr-N bonding as the nitrogen supply increases.

The observed binding energy shift is attributed to improved nitridation and local chemical ordering under nitrogen-rich conditions, facilitated by a higher population of energetic Cr^+/Cr^* species in the HiPIMS process plasma. Although OES provides only qualitative information on excited species, the increase and subsequent stabilization of the Cr^+/Cr^* intensity ratio with increasing N_2 flow correlate well with

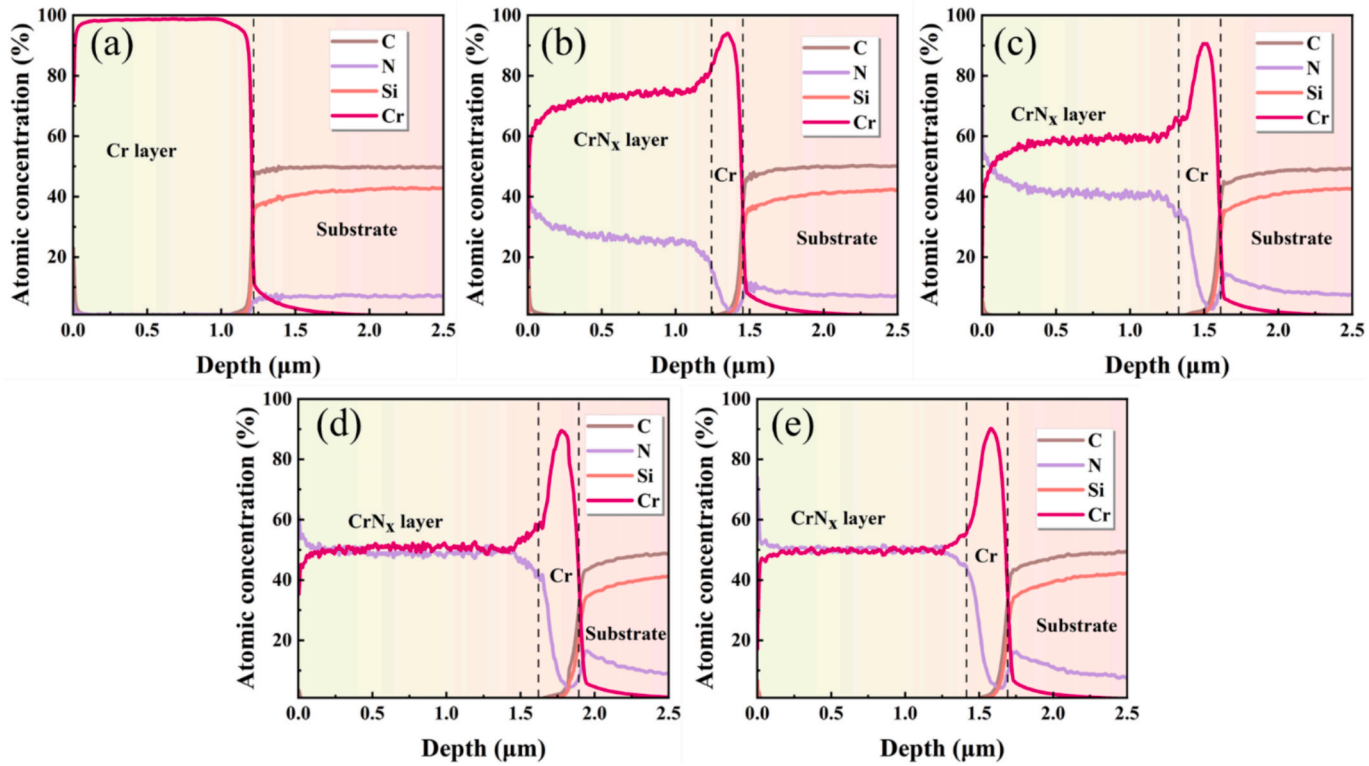

Fig. 7. Chemical composition variation with coating thickness for CrN_x coatings: (a) 0 sccm, (b) 10 sccm, (c) 30 sccm, (d) 55 sccm, and (e) 75 sccm.

the XPS and XRD results. Together, these observations confirm the formation of a stable CrN-dominated growth regime at N_2 flow rates above 30 sccm.

To further investigate the structural evolution of CrN_x coatings under different sputtering modes, the XRD patterns for all samples are presented in Fig. 9. For improved visualization, the intensities of the patterns for 10 sccm and 30 sccm in were scaled down by factors of 0.2 and 0.3, respectively. The phase identification was conducted using PDF card indexes: CrN (No.76-2494), Cr_2N (No.35-0803), and Cr (No.85-1335). As the N_2 flow rate increased, significant changes in the coating's phase structure were observed. At lower N_2 flow rates, the coatings were predominantly composed of the Cr_2N phase. In contrast, at higher N_2 flow rates, CrN phase became dominant, which is consistent with previous studies [36,39,40].

At the N_2 flow rate of 30 sccm, the CrN_x coating exhibits a CrN (2 2 0) preferential orientation, with weaker peaks corresponding to CrN (1 1 1), CrN (2 0 0) and CrN (3 1 1) also detected. As the N_2 flow rate increased from 30 sccm to 75 sccm, the CrN diffraction peaks shifted towards lower Bragg angles. Additionally, the CrN (2 2 0) peak gradually split into two sub-peaks, although not completely resolved [41]. Besides the dominant CrN (2 2 0) peak, an interesting trend is observed for the CrN (2 0 0) reflection, it first intensifies and then weakens with increasing N_2 flow rate.

4. Disscusions

4.1. Discharge behavior and sputtering mode transition in reactive Cr HiPIMS

In reactive magnetron sputtering, the discharge characteristics are governed by the combined effects of target surface condition, gas composition, and plasma properties [42,43]. For Cr-based systems, the formation of nitride compounds such as Cr_2N and CrN on the target surface alters both the sputtering yield and the secondary electron emission characteristics compared to metallic Cr [22]. However, previous study [44] have shown that, although compound formation does not necessarily lead to a drastic reduction in the total sputtering yield, it significantly modifies the discharge behavior through changes in secondary electron emission and surface composition.

In reactive HiPIMS discharges, the discharge behavior exhibits a pronounced hysteresis with increasing and decreasing N_2 flow rates, which is characteristic of reactive sputtering systems. Based on the voltage stability and the shape of the hysteresis loop [45,46], the investigated deposition conditions can be categorized into metallic, transition, and compound sputtering modes. Compared with conventional DC, the discharge characteristics in HiPIMS are further influenced by the high peak currents, Ohmic heating of the plasma, and complex power coupling mechanisms, making the interpretation of voltage and current waveforms inherently multifaceted [47–49]. The observed discharge behavior therefore reflects the combined influence of reactive gas introduction and the intrinsic characteristics of the HiPIMS discharge.

4.2. Plasma characteristics under reactive HiPIMS conditions

The evolution of plasma characteristics with increasing N_2 flow rate provides important insight into the reactive HiPIMS process. OES reveals that the intensities of the dominant detected species, namely Cr* and Ar^+, decrease monotonically as the N_2 flow rate increases. Under constant power operation, the monotonic decrease in OES intensity with increasing N_2 flow rate is commonly associated with progressive target poisoning and the accompanying reduction in secondary electron emission yield, as well as changes in plasma kinetics induced by the participation of nitrogen in the discharge [50]. Under the present measurement conditions, nitrogen-related emission lines could not be clearly resolved, highlighting the qualitative nature of the OES analysis.

The evolution of the Cr^+/Cr^* intensity ratio further reflects changes in plasma excitation and ionization pathways. The higher Cr^+/Cr^* ratios observed in the transition and compound modes indicate that the Cr^+ emission intensity decreases more slowly than that of Cr*, rather than

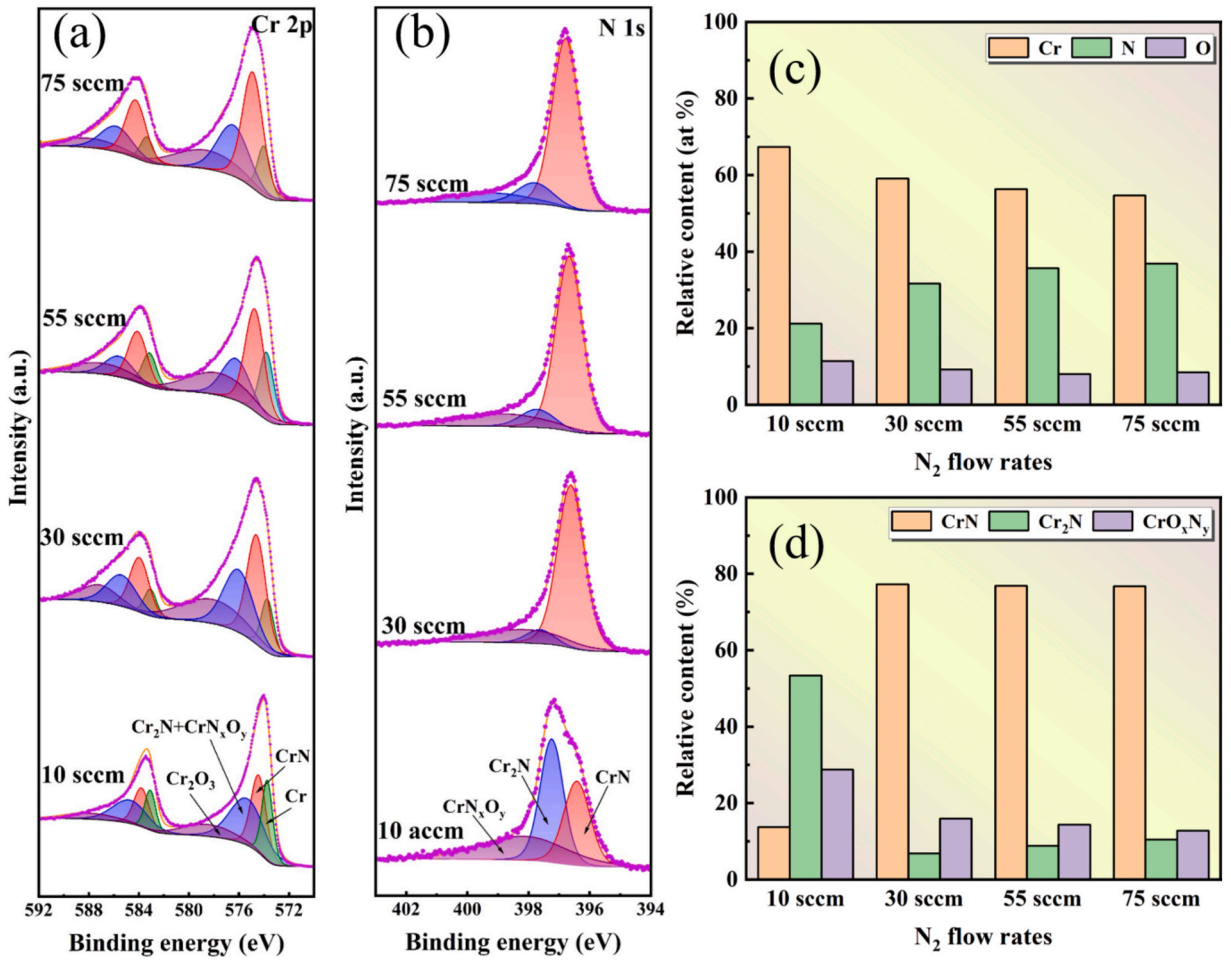

Fig. 8. XPS spectra of CrN_x coatings: (a) the Cr 2p peak, (b) the N 1s peak, (c) surface elemental composition based on XPS quantitative analysis, and (d) relative surface phase composition estimated from peak deconvolution.

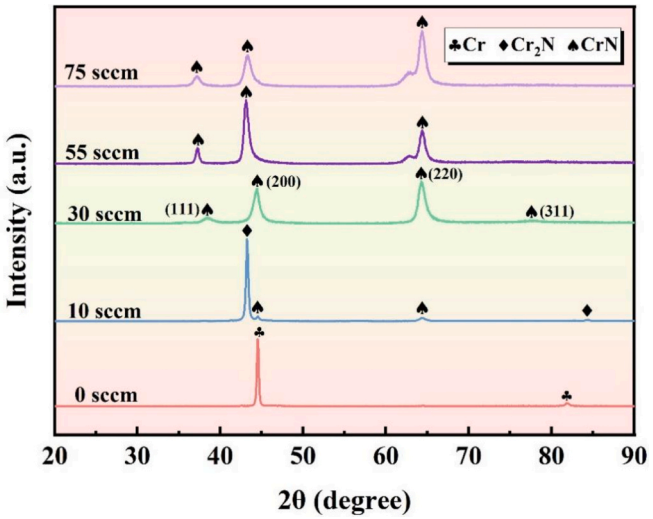

Fig. 9. XRD patterns of CrN_x coatings.

implying an absolute increase in metal ionization. At N_2 flow rates above 30 sccm, the Cr^+/Cr^* intensity ratio remains approximately constant within experimental uncertainty, indicating a stabilized excitation-ionization balance in the transition and compound modes.

This behavior is consistent with the evolution of the peak power density of the reactive HiPIMS discharge, which increases with N_2 flow rate up to 30 sccm and approaches a stable level at higher N_2 flow rates. However, it should be emphasized that OES provides only qualitative information on excited species and does not allow direct determination of absolute ionization efficiencies.

Langmuir probe diagnostics provide complementary insight into the plasma state. The measured electron energy distribution functions exhibit a single-peaked Maxwellian shape with nearly unchanged peak positions in the low-energy region. With increasing N_2 flow rate, however, the population of high-energy electrons becomes progressively enhanced, leading to the development of a pronounced high-energy tail [51]. This behavior is attributed to the introduction of N_2 molecules, which alter the electron energy balance through additional inelastic collision channels, such as excitation and ionization, thereby preferentially depleting low- to mid-energy electrons and reshaping the EEDF [52]. Concurrently, the electron density decreases by approximately one third during the transition from metallic to compound mode, while the effective electron temperature increases. These trends are consistent with the higher discharge voltages required to sustain constant-power operation under nitrogen-rich conditions, as well as with changes in target surface properties associated with nitridation.

4.3. Nitrogen incorporation

The nitrogen incorporation behavior of the CrN_x coatings shows a rapid increase with increasing N_2 flow rate, followed by a clear saturation at high nitrogen supply [53]. EPMA measurements indicate that the

nitrogen content increases markedly and approaches approximately 52 at.% at N_2 flow rates above 55 sccm. In contrast, GD-OES depth profiling yields a nitrogen concentration close to 50 at.% across the coating thickness under the same deposition conditions.

The slight difference between the nitrogen contents measured by EPMA and GD-OES can be attributed to the intrinsic uncertainties and different sampling characteristics of the two techniques. Importantly, within experimental uncertainty, both values are consistent with the stoichiometric nitrogen content of CrN (~50 at.% N) defined by the Cr–N phase diagram. These results indicate that once the CrN-dominated growth regime is established, further increases in nitrogen supply do not lead to nitrogen supersaturation but instead result in a composition constrained by thermodynamic stability.

Surface-sensitive XPS analysis yields lower absolute nitrogen concentrations due to its limited information depth (a few nanometers) and the unavoidable presence of surface oxidation and oxynitride formation upon air exposure [54]. Although Ar^+ sputter cleaning was applied, oxygen-containing species cannot be completely removed from the extreme surface region, leading to an apparent reduction in the measured nitrogen content. Importantly, no significant oxygen was detected by EPMA or GD-OES, confirming that oxidation is confined to the surface and does not affect the bulk composition of the coatings.

Despite these quantitative differences, XPS exhibits the same qualitative trend of increasing nitrogen content with N_2 flow rate and a pronounced saturation behavior. The gradual shift of the N 1s binding energy toward higher values observed by XPS further supports the stabilization of the local Cr–N bonding environment during the transition from metallic to compound sputtering modes [55]. Notably, this evolution occurs predominantly in the same N_2 flow range (10–30 sccm) where the Cr^+/Cr^* intensity ratio derived from OES increases before reaching a stable level at higher N_2 flow rates, indicating a parallel evolution of plasma excitation characteristics and coating growth chemistry. The consistent saturation trends observed by EPMA, GD-OES, and XPS, despite their fundamentally different information depths, provide strong evidence that nitrogen incorporation in the present CrN_x coatings is governed by a stoichiometric limitation.

4.4. Phase and microstructural evolution of CrN_x coatings

The phase evolution observed by XRD is consistent with the nitrogen incorporation behavior discussed above. At low N_2 flow rates, the coatings are dominated by the Cr_2N phase, whereas increasing N_2 flow promotes the formation of CrN, which becomes the dominant phase in the transition and compound sputtering modes.

In addition to phase composition, systematic changes in preferred orientation are observed. The dominance of the CrN (220) reflection together with the non-monotonic evolution of the CrN (200) reflection indicates a competition between different growth orientations as deposition conditions vary. Such competition between the (200) and (220) orientations is well documented for NaCl-type transition metal nitrides deposited under energetic sputtering conditions, where different crystallographic directions exhibit distinct growth stability and ion-surface interaction characteristics [56,57].

The observed shift of the CrN diffraction peaks toward lower Bragg angles, together with the splitting of the CrN (220) peak, is commonly attributed to changes in macroscopic residual stress [58,59] and to lattice distortion induced by the incorporation of excess nitrogen atoms into the octahedral interstitial sites of the face-centered cubic Cr lattice [60]. The columnar microstructure observed by cross-sectional SEM is consistent with deposition at relatively low homologous temperatures, as commonly described by the Structure Zone Model [61]. In addition, a refinement of the columnar structure is observed at higher N_2 flow rates, which coincides with changes in phase constitution and preferred growth orientation under nitrogen-rich conditions.

5. Conclusions

This study investigated the deposition of CrN_x coatings by reactive HiPIMS, with particular emphasis on the interplay between plasma characteristics and nitrogen incorporation behavior. The main conclusions can be summarized as follows:

(1) The nitrogen content in the CrN_x coatings increases with N_2 flow rate and exhibits a pronounced saturation behavior at approximately 52 at.%. Within experimental uncertainty, this saturation level is consistent with the stoichiometric composition of CrN defined by the Cr-N phase diagram, indicating that nitrogen incorporation is ultimately constrained by the thermodynamic composition limit of the Cr-N system.
(2) The evolution toward stoichiometric CrN during reactive HiPIMS deposition is closely associated with the intrinsically high-energy characteristics of the HiPIMS discharge. As the N_2 flow rate increases (0–75 sccm), the peak power density rises, accompanied by an enhanced Cr^+/Cr^* emission intensity ratio, reflecting a plasma state enriched with energetic metal species. This increased energy flux delivered to the growing film promotes stronger Cr-N bonding, as evidenced by the systematic shift of the N 1s binding energy toward higher values in XPS, highlighting the advantage of HiPIMS in enabling energy-assisted nitride growth.
(3) While the thermodynamic limit defines the maximum achievable nitrogen content in the Cr-N system, reactive HiPIMS plays a decisive role in controlling the kinetic pathway toward this limit. By providing a high-energy, metal-ion-dominated plasma environment, HiPIMS facilitates the formation and stabilization of stoichiometric CrN without altering the intrinsic thermodynamic boundary, thereby steering phase formation and bonding configuration through energy-assisted growth kinetics.

In summary, the composition and phase structure of reactive HiPIMS-deposited CrN_x coatings are governed by the interplay between thermodynamic constraints and plasma-assisted kinetics. The thermodynamic limit dictates the attainable stoichiometry, whereas the high peak power density and energetic plasma conditions inherent to HiPIMS provide an effective means to control the kinetic evolution of nitrogen incorporation and Cr-N bonding along the deposition pathway. These findings underscore the potential of reactive HiPIMS as a versatile and energy-efficient technique for tailoring nitride coatings through controlled plasma-surface interactions.

CRediT authorship contribution statement

Kaiwei Yang: Writing – original draft, Investigation, Formal analysis, Data curation, Conceptualization. **Yiqun Feng:** Writing – original draft, Visualization, Validation, Methodology, Conceptualization. **Yuxing Qi:** Validation, Investigation. **Guanshui Ma:** Validation. **Zhenyu Wang:** Supervision, Funding acquisition. **Aiying Wang:** Writing – review & editing, Visualization, Supervision, Funding acquisition, Conceptualization.

Declaration of competing interest

The authors declare that they have no known competing financial interests or personal relationships that could have appeared to influence the work reported in this paper.

Acknowledgments

This work was financially supported by the National Key Research and Development Program of China (2024YFB3816500), the National Science Fund for Distinguished Young Scholars of China (52025014),

and the Key Research and Development Program of Ningbo (2023Z110, 2025Z135, 2024Z154).

Data availability

Data will be made available on request.

References

[1] S.H. Zhou, Z.G. Qiu, Z.Y. Wang, W. Yang, A.Y. Wang, Observation of dislocation-mediated plastic deformation in TiMoN coating, Rare Met. 44 (2025) 2845–2852, https://doi.org/10.1007/s12598-024-03128-3.

[2] J.C. Sánchez-López, A. Caro, G. Alcalá, T.C. Rojas, Tailoring CrNx stoichiometry and functionality by means of reactive HiPIMS, Surf. Coat. Technol. 401 (2020) 126235, https://doi.org/10.1016/j.surfcoat.2020.126235.

[3] Y. Li, C. Hu, Y. Wu, Z. Qiao, Y. Cheng, Z. Gu, G. Gao, W. Zheng, Designing hard wear-resistant conductors by introducing high-plasma-energy heterogeneous metals into transition metal nitrides, J. Mater. Sci. Technol. 157 (2023) 213–219, https://doi.org/10.1016/j.jmst.2023.02.025.

[4] Y. Feng, T.F. Chung, J.H. Huang, Effect of nitrogen flow rate on the mechanical properties of (V,Mo)N thin films, Surf. Coat. Technol. 452 (2023) 129116, https://doi.org/10.1016/j.surfcoat.2022.129116.

[5] T. Narayana, S.S. Saleem, Comparative investigation and characterization of the nano-mechanical and tribological behavior of RF magnetron sputtered TiN, CrN, and TiB2 coating on Ti6Al4V alloy, Tribol. Int. 193 (2024) 109348, https://doi.org/10.1016/j.triboint.2024.109348.

[6] S.K. Tiwari, A.U. Rao, A.S. Kharb, D.K. Avasthi, P.C. Verma, A.K. Chawla, The effect of sputtering parameters and doping on the properties of CrN-based coatings—a critical review, Surf. Interface Anal. 56 (2024) 479–497, https://doi.org/10.1002/sia.7306.

[7] Z. Zhao, Y. Guan, Y. He, Y. Xin, Y. Hu, L. Huang, Q. Shi, C. Deng, Effect of Cr/Zr metal layer on the microstructure and properties of CrN coating deposited by arc ion plating, Surf. Coat. Technol. 516 (2025) 132730, https://doi.org/10.1016/j.surfcoat.2025.132730.

[8] Q. Yang, C. He, L.R. Zhao, J.P. Immarigeon, Preferred orientation and hardness enhancement of TiN/CrN superlattice coatings deposited by reactive magnetron sputtering, Scr. Mater. 46 (2002) 293–297, https://doi.org/10.1016/s1359-6462(01)01241-6.

[9] K. Alam, M.B. Haider, M.F. Al-Kuhaili, K.A. Ziq, B.U. Haq, Electronic phase transition in CrN thin films grown by reactive RF magnetron sputtering, Ceram. Int. 48 (2022) 17352–17358, https://doi.org/10.1016/j.ceramint.2022.02.298.

[10] A. Bousquet, L. Spinelle, J. Cellier, E. Tomasella, Optical emission spectroscopy analysis of Ar/N2 plasma in reactive magnetron sputtering, Plasma Process. Polym. 6 (2009) S605–S609, https://doi.org/10.1002/ppap.200931602.

[11] C.L. Chang, S.G. Shih, P.H. Chen, W.C. Chen, C.T. Ho, W.Y. Wu, Effect of duty cycles on the deposition and characteristics of high power impulse magnetron sputtering deposited TiN thin films, Surf. Coat. Technol. 259 (2014) 232–237, https://doi.org/10.1016/j.surfcoat.2014.03.011.

[12] Y. Feng, T.F. Chung, C.N. Hsiao, J.H. Huang, Effects of duty cycle and nitrogen flow rate on the mechanical properties of (V, Mo) N coatings deposited by high-power pulsed magnetron sputtering, J. Vac. Sci. Technol. A 41 (2023) 063109, https://doi.org/10.1116/6.0003006.

[13] K. Xu, S. Zhou, Z. Wang, X. Sun, K. Yang, K. Wang, A. Wang, P. Ke, Prism-plane-textured Cr2AlC MAX-phase coatings with superior resistance to coupled thermal–salt–steam corrosion, Corros. Sci. 258 (2026) 113395, https://doi.org/10.1016/j.corsci.2025.113395.

[14] V. Layes, C. Corbella, S. Thiemann-Monjé1, V. Schulz-von der Gathen, A. von Keudell1, T. de los Arcos, Connection between target poisoning and current waveforms in reactive high power impulse magnetron sputtering of chromium, Plasma Sources Sci. Technol. 27 (2018) 084004, https://doi.org/10.1088/1361-6595/aad0e2.

[15] D. Boivin, A. Najah, R. Jean-Marie-Désirée, C. Noël, G. Henrion, S. Cuynet, L. De Poucques, Towards control of TiO2 thickness film in R-HiPIMS process with a coupled optical and electrical monitoring of plasma, Surf. Coat. Technol. 433 (2022) 128073, https://doi.org/10.1016/j.surfcoat.2021.128073.

[16] C. Nouvellon, M. Michiels, J.P. Dauchot, C. Archambeau, F. Laffineur, E. Silberberg, S. Delvaux, R. Cloots, S. Konstantinidis, R. Snyders, Deposition of titanium oxide films by reactive High Power Impulse Magnetron Sputtering (HiPIMS): influence of the peak current value on the transition from metallic to poisoned regimes, Surf. Coat. Technol. 206 (2012) 3542–3549, https://doi.org/10.1016/j.surfcoat.2012.02.034.

[17] G. Greczynski, J. Jensen, J. Böhlmark, L. Hultman, Microstructure control of CrNx films during high power impulse magnetron sputtering, Surf. Coat. Technol. 205 (2010) 118–130, https://doi.org/10.1016/j.surfcoat.2010.06.016.

[18] K. Macák, V. Kouznetsov, J. Schneider, U. Helmersson, I. Petrov, Ionized sputter deposition using an extremely high plasma density pulsed magnetron discharge, J. Vac. Sci. Technol. A 18 (2000) 1533–1537, https://doi.org/10.1116/1.582380.

[19] A. Vetushka, A.P. Ehiasarian, Plasma dynamic in chromium and titanium HIPIMS discharges, J. Phys. D Appl. Phys. 41 (2008) 015204, https://doi.org/10.1088/0022-3727/41/1/015204.

[20] X. Zhou, H. Du, G. Ma, Z. Wang, W. Yang, K. Nishimura, P. Guo, A. Wang, P. Ke, HiPIMS-deposited CrxN coatings for marine applications: controllable microstructure and tribocorrosion behavior, Corros. Commun. 20 (2025) 24–32, https://doi.org/10.1016/j.corcom.2024.05.004.

[21] J. Gao, H. Bai, J. Li, Y. Bai, L. Han, J. Ni, X. Liu, Enhanced hardness and plasticity of Cr-CrN coatings with periodic gradient structures, Surf. Coat. Technol. 515 (2025) 132626, https://doi.org/10.1016/j.surfcoat.2025.132626.

[22] D. Depla, S. Mahieu, R. De Gryse, Magnetron sputter deposition: linking discharge voltage with target properties, Thin Solid Films 517 (2009) 2825–2839, https://doi.org/10.1016/j.tsf.2008.11.108.

[23] X. Zuo, D. Zhang, R. Chen, P. Ke, M. Odén, A. Wang, Spectroscopic investigation on the near-substrate plasma characteristics of chromium HiPIMS in low density discharge mode, Plasma Sour. Sci. Technol. 29 (2020) 015013, https://doi.org/10.1088/1361-6595/ab5c03.

[24] G. Zhou, Z. Li, J. Yuan, R. Chen, Z. Wang, P. Ke, A. Wang, Enhanced crystalline growth of Cr2AlC MAX phase coating by hybrid DCMS/HiPIMS, Appl. Surf. Sci. 666 (2024) 160371, https://doi.org/10.1016/j.apsusc.2024.160371.

[25] A. Anders, Discharge physics of high power impulse magnetron sputtering, Surf. Coat. Technol. 205 (2011) S1–S9, https://doi.org/10.1016/j.surfcoat.2011.03.081.

[26] P. Vašina, M. Fekete, J. Hnilica, P. Klein, L. Dosoudilová, P. Dvořák, Z. Navrátil, Determination of titanium atom and ion densities in sputter deposition plasmas by optical emission spectroscopy, Plasma Sour. Sci. Technol. 24 (2015) 065022, https://doi.org/10.1088/0963-0252/24/6/065022.

[27] X. Zuo, R. Chen, J. Liu, P. Ke, A. Wang, The influence of superimposed DC current on electrical and spectroscopic characteristics of HiPIMS discharge, AIP Adv. 8 (2018) 015132, https://doi.org/10.1063/1.5018037.

[28] A.P. Ehiasarian, W.D. Munz, L. Hultman, U. Helmersson, I. Petrov, High power pulsed magnetron sputtered CrNx films, Surf. Coat. Technol. 163 (2003) 267–272, https://doi.org/10.1016/s0257-8972(02)00479-6.

[29] K. Sarakinos, J. Alami, S. Konstantinidis, High power pulsed magnetron sputtering: a review on scientific and engineering state of the art, Surf. Coat. Technol. 204 (2010) 1661–1684, https://doi.org/10.1016/j.surfcoat.2009.11.013.

[30] W. Huber, T. Houlahan, Z. Jeckell, D. Barlaz, I. Haehnlein, B. Jurczyk, D.N. Ruzic, Time-resolved electron energy distribution functions at the substrate during a HiPIMS discharge with cathode voltage reversal, Plasma Sources Sci. Technol. 31 (2022) 065001, https://doi.org/10.1088/1361-6595/ac6d0a.

[31] I. Bertoti, Characterization of nitride coatings by XPS, Surf. Coat. Technol. 151 (2002) 194–203, https://doi.org/10.1016/s0257-8972(01)01619-x.

[32] A. Conde, A.B. Cristóbal, G. Fuentes, T. Tate, J. de Damborenea, Surface analysis of electrochemically stripped CrN coatings, Surf. Coat. Technol. 201 (2006) 3588–3595, https://doi.org/10.1016/j.surfcoat.2006.08.110.

[33] A. Vyas, Z.F. Zhou, Y. G., Effect of aluminum contents on sputter deposited CrAlN thin films, IOP Conf. Ser.: Mater. Sci. Eng. 307 (2018) 012079, https://doi.org/10.1088/1757-899X/307/1/012079.

[34] N. Liu, J. Gao, Y. Li, J. Wang, Y. Wan, R. Li, Different tribological behavior of CrN and CrCuN coatings under glycerol lubrication, Surf. Coat. Technol. 436 (2022) 128262, https://doi.org/10.1016/j.surfcoat.2022.128262.

[35] E. Desimoni, C. Malitesta, P.G. Zambonin, J.C. Riviere, An x-ray photoelectron spectroscopic study of some chromium–oxygen systems, Surf. Interface Anal. 13 (1988) 173–179, https://doi.org/10.1002/sia.740130210.

[36] L. Shan, Y. Wang, J. Li, J. Chen, Effect of N2 flow rate on microstructure and mechanical properties of PVD CrNx coatings for tribological application in seawater, Surf. Coat. Technol. 242 (2014) 74–82, https://doi.org/10.1016/j.surfcoat.2014.01.021.

[37] Y. Li, L. Cao, C. Qi, H. Su, Y. Wan, J. Lv, Low friction of CrN coatings in presence of glycerol, Appl. Surf. Sci. 514 (2020) 145890, https://doi.org/10.1016/j.apsusc.2020.145890.

[38] S. Zhang, M. Li, Y. He, T. Cho, H. Chun, J. Yoon, S. Si, H. Li, Synthesis and properties of CrNx/amorphous-WC nanocomposites prepared using hybrid arc ion plating and direct current magnetron sputtering, Thin Solid Films 519 (2010) 751–758, https://doi.org/10.1016/j.tsf.2010.08.152.

[39] R. Elo, S. Jacobson, T. Kubart, Tailoring residual stresses in CrNx films on alumina and silicon deposited by high-power impulse magnetron sputtering, Surf. Coat. Technol. 397 (2020) 125990, https://doi.org/10.1016/j.surfcoat.2020.125990.

[40] B. Gui, H. Zhou, X. Liu, K. Zhang, H. Hu, L. Yang, Y. Zhang, Influence of N2 flow rate on microstructure and properties of CrNx ceramic films prepared by MPP technique at low temperature, Ceram. Int. 47 (2021) 20875–20884, https://doi.org/10.1016/j.ceramint.2021.04.086.

[41] X.L. Li, X. Jiang, W. Lia, X.J. Zhou, Y. Wang, Y. Chen, C. Xiong, F. You, X. Li, L. T. Liu, Effect of different N contents on CrN coatings of aluminium alloy bipolar plates for proton exchange membrane fuel cells, Ceram. Int. 51 (2025) 3546–3558, https://doi.org/10.1016/j.ceramint.2024.11.331.

[42] Y.P. Purandare, A.P. Ehiasarian, P. Eh Hovsepian, Target poisoning during CrN deposition by mixed high power impulse magnetron sputtering and unbalanced magnetron sputtering technique, J. Vac. Sci. Technol. A 34 (2016) 041502, https://doi.org/10.1116/1.4950886.

[43] A. Anders, Tutorial: reactive high power impulse magnetron sputtering (R-HiPIMS), J. Appl. Phys. 121 (2017) 34, https://doi.org/10.1063/1.4978350.

[44] J. Van Bever, K. Strijckmans, S. Konstantinidis, D. Depla, Convergence during feedback controlled reactive magnetron sputtering: mechanisms and classification, Surf. Coat. Technol. 507 (2025) 132095, https://doi.org/10.1016/j.surfcoat.2025.132095.

[45] J. Musil, P. Baroch, J. Vlček, K.H. Nam, J.G. Han, Reactive magnetron sputtering of thin films: present status and trends, Thin Solid Films 475 (2005) 208–218, https://doi.org/10.1016/j.tsf.2004.07.041.

[46] E. Haye, F. Capon, S. Barrat, D. Mangin, J.-F. Pierson, Phenomenological study of iron and lanthanum magnetron co-sputtering using two reactive gases, Surf. Coat. Technol. 298 (2016) 39–44, https://doi.org/10.1016/j.surfcoat.2016.04.039.
[47] A. Anders, Glows, arcs, ohmic discharges: an electrode-centered review on discharge modes and the transitions between them, Appl. Phys. Rev. 11 (2024) 031310, https://doi.org/10.1063/5.02050274.
[48] S. Pandey, D.N. Patel, A.R. Baitha, S. Bhattacharjee, Particle energy distributions and metastable atoms in transient low pressure interpulse microwave plasma, Plasma Sources Sci. Technol. 24 (2015) 065004, https://doi.org/10.1088/0963-0252/24/6/065004.
[49] M. Rudolph, N. Brenning, H. Hajihoseini, M.A. Raadu, J. Fischer, J. T. Gudmundsson, D. Lundin, Operating modes and target erosion in high power impulse magnetron sputtering, J. Vac. Sci. Technol. A 40 (2022) 043005, https://doi.org/10.1116/6.0001919.
[50] B.-S. Lou, W.-T. Chen, W. Diyatmika, J.-H. Lu, C.-T. Chang, P.-W. Chen, J.-W. Lee, Effect of target poisoning ratios on the fabrication of titanium oxide coatings using superimposed high power impulse and medium frequency magnetron sputtering, Surf. Coat. Technol. 421 (2021) 127430, https://doi.org/10.1016/j.surfcoat.2021.127430.
[51] K.-Y. Kim, J.H. Kim, C.-W. Chung, H.-C. Lee, Effect of electron energy distributions on the electron density in nitrogen inductively coupled plasmas, Plasma Sources Sci. Technol. 31 (2022) 105007, https://doi.org/10.1088/1361-6595/ac942b.
[52] H. Singh, D.B. Graves, Measurements of the electron energy distribution function in molecular gases in an inductively coupled plasma, J. Appl. Phys. 87 (2000) 4098–4106, https://doi.org/10.1063/1.373036.
[53] S. Berg, T. Nyberg, Fundamental understanding and modeling of reactive sputtering processes, Thin Solid Films 476 (2005) 215–230, https://doi.org/10.1016/j.tsf.2004.10.051.
[54] J. Liu, J.-P. Glauber, J. Lorenz, D. Rogalla, C. Harms, A. Devi, M. Nolan, Surface oxidation of transition metal nitrides, J. Phys. Chem. C 129 (2025) 11173–11182, https://doi.org/10.1002/smtd.202501972.
[55] L. Aissani, M. Fellah, A.H. Chadli, M.A. Samad, A. Cheriet, F. Salhi, C. Nouveau, S. Weiß, A. Obrosov, A. Alhussein, Investigating the effect of nitrogen on the structural and tribo-mechanical behavior of vanadium nitride thin films deposited using R.F. magnetron sputtering, J. Mater. Sci. 56 (2021) 17319–17336, https://doi.org/10.1007/s10853-021-06393-0.
[56] D. Dobrev, Ion-beam-induced texture formation in vacuum-condensed thin metal films, Thin Solid Films 92 (1982) 41–53, https://doi.org/10.1016/0040-6090(82)90186-9.
[57] G.N. Van Wyk, H.J. Smith, Crystalline reorientation due to ion bombardment, Nucl. Instrum. Methods 170 (1980) 433–439, https://doi.org/10.1016/0029-554X(80)91053-8.
[58] J.D. Castro, B. Pinto, F. Ferreira, R. Serra, S. Carvalho, Wettability and corrosion resistance of zirconium nitride films obtained via reactive high-power impulse magnetron sputtering, J. Vac. Sci. Technol. A 41 (2023) 023106, https://doi.org/10.1116/6.0002341.
[59] Q. Chen, H. Yang, L. Wu, X. Wu, C. Zhu, L. He, N. Liu, Y. Yang, J. Liao, J. Yang, Effect of the Ar/N2 flow ratio on the microstructure, mechanical properties, and high-temperature steam oxidation behavior of Cr/CrxN coatings for accident-tolerant fuel coatings, Corros. Sci. 192 (2021) 109833, https://doi.org/10.1016/j.corsci.2021.109833.
[60] F. Ferreira, J.C. Oliveira, A. Cavaleiro, CrN thin films deposited by HiPIMS in DOMS mode, Surf. Coat. Technol. 291 (2016) 365–375, https://doi.org/10.1016/j.surfcoat.2016.02.064.
[61] D. Zhang, X. Zuo, Z. Wang, H. Li, R. Chen, A. Wang, P. Ke, Comparative study on protective properties of CrN coatings on the ABS substrate by DCMS and HiPIMS techniques, Surf. Coat. Technol. 394 (2020) 125890, https://doi.org/10.1016/j.surfcoat.2020.125890.